

# High-throughput Li plating quantification for fast-charging battery design

Zachary M. Konz<sup>1,2</sup>, Brendan M. Wirtz<sup>1\*</sup>, Ankit Verma<sup>3</sup>, Tzu-Yang Huang<sup>1,2</sup>, Helen K. Bergstrom<sup>1,2</sup>,  
Matthew J. Crafton<sup>1,2</sup>, David E. Brown<sup>1,2</sup>, Eric J. McShane<sup>1,2\*</sup>, Andrew M. Colclasure<sup>3</sup>, Bryan D.  
McCloskey<sup>1,2</sup>

1. Department of Chemical and Biomolecular Engineering, University of California, Berkeley, Berkeley, CA, USA
  2. Energy Storage and Distributed Resources Division, Lawrence Berkeley National Laboratory, Berkeley, CA, USA
  3. Energy Conversion and Storage Systems Center, National Renewable Energy Laboratory, Golden, CO, USA
- \* Present address: Department of Chemical Engineering, Stanford University, Stanford, CA, USA

## Abstract

Fast charging of most commercial lithium-ion batteries is limited due to fear of lithium plating on the graphite anode, which is difficult to detect and poses significant safety risk. Here we demonstrate the power of simple, accessible, and high-throughput cycling techniques to quantify irreversible Li plating spanning data from over 200 cells. We first observe the effects of energy density, charge rate, temperature, and State-of-Charge (SOC) on lithium plating, use the results to refine mature physics-based electrochemical models, and provide an interpretable empirical equation for predicting the plating onset SOC. We then explore the reversibility of lithium plating and its connection to electrolyte design for preventing irreversible Li accumulation. Finally, we design a method to quantify in-situ Li plating for commercially relevant Graphite|LiNi<sub>0.5</sub>Mn<sub>0.3</sub>Co<sub>0.2</sub>O<sub>2</sub> (NMC) cells and compare with results from the experimentally convenient Li|Graphite configuration. The hypotheses and abundant data herein were generated primarily with equipment universal to the battery researcher, encouraging further development of innovative testing methods and data processing that enable rapid battery engineering.

## 30 Introduction

31

32 The urgent need to combat climate change has sparked extreme growth in demand for lithium-ion  
33 batteries (LIB). Rapid innovation in battery materials and cell design is critical to meet this demand for  
34 diverse applications from electronics to vehicles and utility-scale energy storage. Composite graphite  
35 electrodes remain a universal component of the LIB and are expected to dominate anode market share  
36 through 2030 despite the introduction of silicon and lithium-based materials<sup>1</sup>.

37

38 The design space for graphite electrodes is immense, with parameters such as the loading, porosity,  
39 particle size, binder composition, and electrolyte being carefully selected to meet requirements for  
40 lifetime, operating temperature, charge time, and manufacturing. Regardless of design and application,  
41 the lithium plating reaction on graphite is a performance and safety concern due to the formation of non-  
42 cyclable ‘dead’ lithium metal and salts. While recent studies have focused on Li plating during fast  
43 charging, the phenomenon is also pertinent to other operating extremes such as low temperature<sup>2</sup>,  
44 overcharge<sup>3</sup>, or system malfunction<sup>4</sup>.

45

46 Electrochemical (EChem) modeling is an important tool for understanding design tradeoffs that improve  
47 graphite performance while avoiding plating. Over decades, Newman-based models that relate cell  
48 current density, voltage, temperature, and material properties to graphite intercalation have been  
49 enhanced to also estimate lithium plating.<sup>5-10</sup> This has led to initial insight into the effect of charge rate,  
50 electrode loading, and temperature on lithium plating onset/amount, but simulations rely on debated  
51 parameters such as the plating exchange current density or reversibility and are frequently not verified  
52 with direct experimental measurements<sup>11</sup> such as Li gas evolution titrations<sup>12,13</sup>. EChem models also  
53 have limited ability to predict the chemical compatibility and interphasial properties for novel  
54 electrolytes. High-throughput modeling advances for battery materials and interfaces could fill this void,  
55 but they too lack commensurate validation<sup>14</sup>.

56

57 Challenges to high-throughput battery testing can include limited access to expensive equipment, slow  
58 multiweek cycling tests, limited material availability, high labor cost of cell assembly, complex analysis  
59 methods, and inefficient data handling. There are promising solutions to some of these problems. To  
60 conserve newly synthesized electrode materials, it is common practice to determine charge rate  
61 capabilities by testing multiple rates on a single cell<sup>15,16</sup>. High-precision coulometers have been developed  
62 to improve early performance prediction<sup>17,18</sup>. Data-driven models that predict cycle life from minimal  
63 data<sup>19</sup> can be used to quickly optimize charge protocols<sup>20</sup>, although large data sets are difficult to obtain  
64 in most laboratory settings<sup>21</sup>.

65

66 Here we demonstrate the power of simple, quantitative, and accessible cycling protocols to inform  
67 battery design for Li plating-free charging. The tradeoffs between energy density, charge rate, charge  
68 temperature, and lithium plating are experimentally quantified and used to refine mature electrochemical  
69 models. We then explore the reversibility of lithium plating under varied fast charging conditions, and  
70 apply our understanding towards development of electrolytes and interfaces that limit dead Li formation.  
71 We emphasize that the hypotheses and abundant data presented herein were generated primarily with  
72 equipment universal to the battery researcher, enabled by strategic data handling, while the sophisticated  
73 modeling and titration techniques were reserved for secondary support of the findings.

74

## 75 Irreversible Li mapping and modeling

76

77 Past independent titration studies of Li plating on copper<sup>12</sup> and graphite<sup>13</sup> both show a strong positive  
78 correlation between coulombic inefficiency and inactive Li<sup>0</sup>, with the majority of the irreversible plating  
79 capacity attributed to H<sub>2</sub>-evolving dead Li species (Li<sup>0</sup>, Li<sub>x</sub>C<sub>6</sub>) for liquid carbonate-based electrolytes.  
80 This observation combined with the high-throughput, precise nature of Li|Graphite cell coulombic  
81 efficiency (CE) measurements motivated the protocol in Figure 1 to estimate irreversible Li plating as a  
82 function of charge length. We define irreversible Li as the sum of irreversibly formed species during Li  
83 plating such as isolated metallic lithium and Li<sup>+</sup>-containing solid-electrolyte interphase (SEI). After  
84 formation cycling (see Methods), the 4C charge capacity is increased stepwise by 5% State-of-Charge  
85 (SOC), or normalized graphite capacity, for each cycle from 10% to 55% SOC (Fig. 1a). Here we refer  
86 to graphite intercalation as ‘charge’ despite the decreasing cell voltage in the Li|Gr half-cell  
87 configuration. We previously demonstrated this ‘SOC-sweep’ approach to study plating with differential  
88 voltage analysis<sup>22</sup>, and a similar stepwise capacity cycling has been used for Gr|Cathode full-cells<sup>23</sup>, but  
89 here we first focus on half-cells due to the stable potential of the Li counter electrode and desire to  
90 isolate graphite anode degradation effects.

91

92 The CE for each of the cycles is shown vs charge capacity in Figure 1b. To estimate the irreversible Li, a  
93 high-efficiency baseline CE (dashed line) is first assigned to the data points at low SOC, where we  
94 attribute the non-unity values to continued SEI formation or slow cell degradation processes rather than  
95 Li plating. CE data are then subtracted from these baselines, ranging 99.85-99.98% (see Fig. S1), to  
96 yield a coulombic inefficiency (CIE) from Li plating-related degradation. The CIE multiplied by the  
97 SOC for each cycle gives irreversible plating capacities as a percent of each cell’s experimental  
98 capacity, which are shown in Fig. 1c for various rates, with the result of each cell represented by a set of  
99 connected data points. Throughout this work, we point out ways that cycling data, modeling, and  
100 titrations further confirm the reliability of CIE for irreversible Li plating quantification. To start, Fig. 1c  
101 data reproducibly shows the expected trend of earlier SOC onsets for Li plating as the rate of fast  
102 charging is increased from 2C to 6C. Supplementary Information Figs. S2-S3 discuss protocol  
103 development, SOC range selection, and control experiments that show minimal cell aging effects for the  
104 SOC-sweep method, whereas Fig. S4 supports the link between CIE and irreversible plating.

105

106 Increasing the charge temperature is a well-known operating control to avoid lithium plating but, to the  
107 best of our knowledge, no work has simultaneously quantified the effects across charge rates (C-rates),  
108 loadings, and SOC, all relevant for battery design. Figure 2a-f shows the irreversible Li plating  
109 estimated from the high-throughput SOC-sweep for graphite loadings of 3.1 mAh/cm<sup>2</sup> (a-c) and 2.1  
110 mAh/cm<sup>2</sup> (d-f) at each of 25°C, 35°C, and 45°C. The data points are experimental averages and the  
111 shaded regions are constructed from the standard deviations calculated at each SOC; the averaging  
112 process is illustrated by comparing Fig. 1c and Fig. 2a. The technique fidelity is supported by  
113 experimental trends that are universally consistent with the expectation that the starting SOC of lithium  
114 plating should be postponed with decreasing current rates (left to right within panels), decreasing  
115 loadings (left to right across panels), and increasing temperature (top to bottom), as seen in shifting  
116 irreversible Li curves in the x-direction.

117

118 Irreversible Li estimates from a previously reported Newman EChem model<sup>19,24-26</sup> are overlaid with  
119 experiment in Figs. 2a-f. The lithium plating reaction is modeled using the formulation proposed by Ren  
120 et al.<sup>8</sup>, with a plating exchange current density of 10 A/m<sup>2</sup> and fixed plating reversibility of 70%, both  
121 estimated using titrations and voltage profiles from an experiment with similar Li plating conditions  
122 (electrode, charge rate, electrolyte, and Li plating capacities)<sup>13</sup> to the present study. Specific parameters  
123 for these electrodes and electrolyte transport properties have been extensively reported and are in Table

124 S3 along with experimental and modeled voltage profiles in Figs. S5 and S6. The excellent qualitative  
125 agreement in irreversible Li curve shape between model and experiment increases confidence in both the  
126 exponential Butler-Volmer kinetic expression used for lithium plating/stripping as well as the  
127 assumption that experimental capacity loss is mostly due to irreversible Li instead of other slower  
128 degradation processes.

129  
130 From this dataset we extract the SOC at which irreversible Li starts to form, or ‘plating onset’, as a  
131 metric to inform safe charge durations and assess the quality of our experiment-model agreement. Here  
132 we define the plating onset threshold as 0.05% irreversible Li, or 1.0-1.5  $\mu\text{Ah}/\text{cm}^2$  for the respective  
133 electrode loadings, which is represented by the horizontal lines in Figs. 2a-f. This is the lowest value  
134 after which clear plating increases are observed and also avoids uncertainty from experimental noise at  
135 low SOC (Fig. 2d, bottom left). The SOC at which plating begins for all 20 conditions are shown in  
136 Figure 2g. Reasonably linear relationships between onset and C-rate are observed at a given temperature  
137 and loading. Additionally, experiment uniquely shows that temperature has nearly double the effect on  
138 plating onsets for the higher loading electrodes than lower loading electrodes (3.1 vs. 2.1  $\text{mAh}/\text{cm}^2$ ), as  
139 indicated by the larger vertical shift in the curves. Physically, this could mean that for the thin electrodes  
140 with onsets above 50% SOC, the accumulation of bulk  $\text{Li}_1\text{C}_6$  and its low open-circuit potential  
141 throughout the electrode promotes lithium deposition regardless of improved Li transport or  
142 intercalation kinetics with temperature. In the thicker electrodes with plating at low SOC, the strong  
143 temperature effect suggests that porous electrolyte  $\text{Li}^+$  transport determines Li plating by controlling the  
144 uniformity of graphite lithiation and therefore the SOC at which  $\text{Li}_1\text{C}_6$  forms at the graphite|separator  
145 interface<sup>24</sup>. These explanations are consistent with optical microscopy that shows Li plating first appears  
146 on top of gold-colored  $\text{Li}_1\text{C}_6$  particles<sup>27</sup>.

147  
148 In general, the EChem model (dashed lines, Fig. 2g) accurately captures the onset of lithium plating with  
149 less than 5% SOC error. Model predictions matched experiment best by slightly modifying graphite  
150 properties from those previously reported<sup>9,24</sup>, such as lowering the activation energy for solid-state  
151 diffusion from 30 kJ/mol to 15 kJ/mol (Fig. S9). We believe this indicates a need to explicitly determine  
152 the diffusion coefficient as a function of lithiation and temperature. At high temperatures, loadings, and  
153 charge rates (2b-ii, upper right), the model predicts lithium plating 5-10% SOC earlier than measured,  
154 and for low loadings (2b-i), the model predicts larger temperature sensitivity than measured. This could  
155 be related to changes in SEI composition/resistivity with elevated temperatures, complex graphite phase  
156 behavior, or diffusion enhancement with rate<sup>28</sup>, none of which are captured by the model. Another  
157 important insight from the experiments is that, like the model predicts, the shape of the irreversible Li  
158 curve is similar near the plating onset regardless of rate, temperature, and loading, indicating some  
159 universal physics of Li plating behavior (Fig. S10). Additionally, the experiment uniquely shows that the  
160 higher-loading electrode tends to promote faster accumulation of irreversible Li, which is likely due to  
161 higher local current densities near the separator that promote faster, more dendritic – and thus more  
162 irreversible – Li plating. The low graphite lithiation (SOC) at these onsets could also promote more  
163 rapid Li metal dissolution, which supports  $\text{Li}^+$  re-intercalation into the graphite after charge<sup>29,30</sup>, making  
164 remaining Li deposits more susceptible to electrical isolation.

165  
166 Given that the plating onset varies somewhat linearly with changes in other variables, we propose an  
167 empirical equation, separate from the physics-derived EChem model, to relate the variables as a step  
168 towards data-driven Li plating models. The plating onset SOC,  $y$ , is written as a linear function of the C-  
169 rate ( $c$ ), loading ( $x$ ), and temperature ( $T$ ), with coefficients  $\alpha$ ,  $\beta$ , and  $\gamma^*$  respectively, and intercept  $\varepsilon$   
170 (Eqn. 1). The  $(1-y)$  correction for  $\gamma$  within  $\gamma^*$  was added to account for the variable temperature effect  
171 with loading in Fig. 2g, noting that  $T$  has a smaller impact for plating onsets at higher onset SOC.  
172 Rearrangement to solve for  $y$  yields Eqn. 2. Applying the empirical fitting to the 20 [ $y$ ,  $c$ ,  $x$ ,  $T$ ] plating

173 onset pairs with 4 parameters unsurprisingly gives a much-improved onset prediction compared to the  
174 Newman model (Fig. 2h), and nearly 60% reduction in the residual sum of squared errors (SSE). Table 1  
175 highlights the benefits for interpreting the data using an analytically differentiable equation, which can  
176 provide heuristics for how Li plating should vary with design parameter changes. Starting from 30°C,  
177 3.1 mAh/cm<sup>2</sup>, and 4C rate, for example, a 1C rate increase would cause a 9% SOC earlier plating onset  
178 and a 1°C increase would postpone the onset 0.7% SOC. This analysis complements recent work that  
179 found a linear correlation between the plating onset and electrode ionic resistance, elucidating the effects  
180 of electrode structure and loading<sup>31</sup>. We also investigated the model's predictive capabilities by studying  
181 a graphite electrode with identical composition but 3.75 mAh/cm<sup>2</sup> loading, well above the previous  
182 experimental range, and observe that it impressively predicts the plating onset within 4% SOC at  
183 moderate rates and temperatures (Fig. S11). Finally, the equation is useful for visualizing battery design  
184 tradeoffs, and Fig. S12a shows the charging temperature required to avoid plating for a constant-current  
185 (CC) charge to 40% SOC for various combinations of rates and loadings. Additional visualizations of  
186 the empirical fitting and a discussion of its limitations are in Fig. S12b-d and Note S3.

$$(1) y(c, x, T) = \alpha c + \beta x + \gamma^* T + \varepsilon \quad \text{where } \gamma^* = \gamma (1 - y)$$

$$(2) y(c, x, T) = \frac{\alpha c + \beta x + \gamma T + \varepsilon}{1 + \gamma T}$$

### 191 Electrolyte discovery to reduce irreversible Li

192  
193 Lithium plating is harmful because the reaction is poorly reversible, which causes loss of cell lithium  
194 inventory, capacity fade, and accumulation of reactive metallic lithium. While the impact of electrolyte  
195 on reversibility is at the forefront of Li metal battery research<sup>32</sup>, few have considered electrolyte  
196 engineering as a plating control strategy for graphite anodes under fast charging. If the reversibility of  
197 plating could be improved from 70% to 90%, for example, then the amount of irreversible plating would  
198 be decreased by a factor of 3 (30% to 10%), drastically reducing the impact on performance and safety.  
199 In this section, we quantify irreversible Li for different electrolytes using the SOC-sweep of Figs 1-2,  
200 demonstrate a rigorous method to estimate plating reversibility on graphite, and argue that plating  
201 reversibility is an important electrolyte design criteria for fast charging.

202  
203 Figure 3a shows the effect of swapping ethylene carbonate (EC) for varied weight percent (wt%)  
204 fluoroethylene carbonate (FEC) on irreversible plating. These compositions were inspired by Li metal  
205 battery studies that repeatedly show FEC can decrease dead Li formation<sup>12,33</sup>. The notable shift in the  
206 curve from 0% to 5% FEC indicates a delayed onset of lithium plating, and the decreasing slopes with  
207 increasing FEC suggest a beneficial concentration effect for reducing dead Li. This observation arises  
208 despite decreasing bulk electrolyte conductivity with increasing FEC (Fig. S13), which led us to  
209 hypothesize that enhanced interfacial properties or fractional plating reversibility may alternatively  
210 explain this result.

211  
212 To systematically explore whether Li plating reversibility plays a role in improved performance with  
213 FEC, we sought a rigorous high throughput method to quantify the value at conditions relevant to fast  
214 charging. The estimation of plating reversibility on graphite at standard SOC (below 100%) and ambient  
215 temperatures is challenging due to the rapid dissolution of reversible Li deposits that supports Li<sup>+</sup> re-  
216 intercalation into the graphite.<sup>27,29,30</sup> A workaround to this is to study plating during graphite overcharge  
217 (above 100% SOC)<sup>34,35</sup>, which has also emerged in the context of hybrid graphite/lithium anodes<sup>36-38</sup>,  
218 but reversibility estimates have only been reported at low current rates (< 0.5C) and/or are deduced from  
219 qualitative voltage plateau transitions.

220

221 The framework we apply to carefully and efficiently estimate the reversibility of Li plating ( $\eta$ ) on  
 222 graphite during fast charge is summarized in Figure 3b. After formation cycling, the first step is to  
 223 estimate the coulombic efficiency for graphite intercalation ( $CE_{int}$ ) without lithium plating (Fig. 3b  
 224 ‘Baseline Cycle’, value  $\sim 99.7\%$  see Table S4). Next, that same cycle is repeated with an added  
 225 overcharge step to induce a known capacity of lithium plating,  $P$ . The capacity lost due to lithium  
 226 plating is then isolated by subtracting the baseline capacity loss of intercalation from the total  
 227 irreversible capacity from the overcharge cycle ( $Q_{irrev}$ , Fig. 3b), which allows the calculation of  $\eta$  from  
 228 Equation 3. Repeating the overcharge cycle 4x on the same cell gives reproducible calculated  
 229 reversibility values for the first three overcharge cycles, increasing confidence in the method and  
 230 allowing error bar estimation with a single cell (see Fig. S14).

$$(3) P(1 - \eta) = Q_{irrev} - (1 - CE_{int})Q_{int}$$

234 Figure 3c shows the calculated lithium plating reversibility for various FEC-containing electrolytes  
 235 when the overcharge amount is varied at a fixed 4C rate (left) and the deposition rate is varied at 20%  
 236 overcharge (right). The plating overcharge amount is defined as the percentage of total graphite capacity  
 237 (here,  $3.1 \text{ mAh/cm}^2$ ) that the electrode is charged beyond complete lithiation. For all conditions, FEC-  
 238 free electrolyte exhibits the lowest  $\eta$ , ranging between 74-91%, and for all electrolytes, the expected  
 239 trends of decreasing  $\eta$  with increasing plating amount and rate are apparent. The beneficial  
 240 concentration effect in FEC-containing electrolytes from Fig. 3a is again observed with the exception of  
 241 low-rate or low-amount conditions, circled in Fig. 3c. We ascribe this observation to plating occurring  
 242 primarily beneath the graphite SEI<sup>39</sup>, which we believe has similar composition across concentrations  
 243 due to overlapping differential capacity curves during the first graphite intercalation (Fig. 3d) when the  
 244 majority of SEI is formed.

246 Finally, we try to connect these  $\eta$  determined from overcharge experiments to the true  $\eta$  range observed  
 247 during fast charging. In the latter, plated lithium is observed within microns of the graphite/separator  
 248 interface<sup>25,40</sup> due to developed concentration and potential gradients, but the overcharge protocol differs  
 249 because it begins without gradients and thus should initially yield more uniform Li deposition, as  
 250 imaged at low rates<sup>37</sup>. Consequently, Figure 3e is a sketch of how lithium plating likely accumulates  
 251 during 4C overcharge, a hypothesis consistent with intuition about gradient development, effective  
 252 porosity decreasing as Li deposits grow, and the observed decrease in  $\eta$  with plating amount as these  
 253 effects lead to higher local current densities and non-uniform deposits near the separator interface. To  
 254 better understand the effect of location on  $\eta$ , an incremental plating reversibility  $\Delta\eta$  for each subsequent  
 255 10% of plating is calculated directly from data in Fig. 3c (see Methods) and shown in Fig. 3f. An  
 256 interesting feature arising from this analysis is that for 30% overcharge, the reversibility for the final  
 257 segment of plating  $\Delta\eta_{20-30}$  is drastically lower for the 0 and 5% FEC electrolytes, suggesting that the  $\eta$   
 258 for the 10% overcharge experiment, equivalent to  $\Delta\eta_{0-10}$ , is artificially high due to uniform plating  
 259 deposition throughout the electrode. The 10-15% FEC samples, in comparison, show less performance  
 260 decline with plating amount, perhaps due to bulk electrolyte effects such as enhanced  $\text{Li}^+$  solvation by  
 261 FEC<sup>41</sup>. As depicted by the Fig. 3e diagram, this last plating segment may occur in a planar manner after  
 262 protruding through the graphite SEI, with growth constrained by the separator. Thus, we might expect  
 263 comparable reversibility for Li plating on a planar substrate such as copper foil, and indeed similar  
 264 trends are observed using identical plating amounts and current densities (Fig. 3f, see Fig. S15 for  
 265 details).

267 Despite the illustrative range of possible plating reversibilities, it remains unclear which is most  
 268 representative of plating under standard charging conditions, i.e. which can best predict irreversible Li  
 269 with models or quantify electrolyte improvements. Leveraging our comprehensive experimental and

270 modeling datasets for the 0% FEC electrolyte, we determine the single  $\eta$  that minimizes the plating  
271 onsets error across all conditions (Fig. 3g, Figs. S7-S8). The  $\eta$  from this analysis is 80%, but most  
272 importantly, the SSE divergence above 90% provides strong evidence that the plating reversibility does  
273 not exceed this value in practice, highlighting the need for careful interpretation of overcharge plating  
274 data. Looking at 0% FEC data in Fig. 3f,  $\eta=80\%$  is between the values for  $\Delta\eta_{0-10}$  and  $\Delta\eta_{10-20}$ ,  
275 suggesting that – if an average of the  $\Delta\eta_{0-10}$  and  $\Delta\eta_{10-20}$  values are representative of true plating  
276 reversibility – this electrolyte would produce 2-3x as much irreversible lithium ( $1-\eta$ ) compared with the  
277 FEC electrolytes (for 5-15% FEC, average  $\Delta\eta$  are 88-93%). Holistically, this evidence suggests that  $\eta$  is  
278 an important electrolyte/interphasial design property for systems susceptible to Li plating. Going  
279 forward, we expect the technique of Fig. 3b to be useful for characterizing additional electrolytes and  
280 assessing innovative methods to mitigate irreversible plating such as separator design<sup>42</sup>.

281

## 282 Full-cells Li plating quantification

283

284 This section first shows that previous half-cell plating onset and electrolyte studies are valuable for  
285 informing commercial full-cell design, which instead use a porous, high-voltage cathode material with  
286 limited lithium inventory. Next, ex-situ titrations are used to verify Li plating and identify cycling data  
287 features from full-cells that are quantitative predictors of plating. Finally, the insights are applied to  
288 design a validated, highly sensitive, in-situ method for Li plating quantification.

289

290 To compare lithium plating behavior across electrolyte compositions, a Graphite|LiNi<sub>0.5</sub>Mn<sub>0.3</sub>Co<sub>0.2</sub>O<sub>2</sub>  
291 (NMC532) was cycled 140 times, alternating 5 moderate 1C CCCV (constant current constant voltage)  
292 charging cycles to 4.2V, holding until C/5 current, with 2 6C CCCV fast charging cycles to 4.2V,  
293 holding until 80% capacity. We selected this protocol to help isolate fast charging-related capacity loss,  
294 expected only during the 6C cycles, from other cell aging effects such as FEC degradation<sup>43</sup>. Figure 4a  
295 shows that the 5-15% FEC full-cells, similar to half-cells, outperform the FEC-free electrolyte,  
296 undergoing on average only about 30% of the capacity fade over the 100 1C cycles, with similar 6C  
297 CCCV charge times compared to 0% FEC (Figs. S21-20). The 2% FEC electrolyte, included for the  
298 common use of FEC as an additive, performed only slightly worse than the higher concentrations. From  
299 our Li reversibility analysis, the lack of a clear concentration effect on performance may indicate small  
300 amounts of plating occurring mostly beneath the FEC-derived SEI. It may also indicate the importance  
301 of SEI in delaying the plating onset SOC, which is seen in Fig. 3a and suggested by others<sup>44</sup> to explain  
302 better rate performance with an artificial graphite SEI coating. Significant sample variability is expected  
303 due to the heterogeneous nature of lithium plating and is depicted by the representative error bars  
304 obtained from replicate trials on multiple cells.

305

306 We then use the cycling data to quantify degradation from fast charging and compare results with Li  
307 titrations of the extracted electrodes. Others have reported that irreversibly plated lithium is linearly  
308 correlated to cell capacity loss<sup>45</sup>, so we expect the abrupt capacity changes after the 6C cycles (Fig. 4a,  
309 box) to correlate with titrated Li capacity from mass spectrometry titration (MST). MST<sup>13</sup> accurately  
310 quantifies the combined H<sub>2</sub>-evolving species on graphite such as isolated ‘dead’ Li<sup>0</sup> and inactive Li<sub>x</sub>C<sub>6</sub>  
311 with exceptional resolution (see Methods). However, the titrated Li slightly exceeds the capacity loss for  
312 most of the 0% FEC samples despite controls that show minimal Li<sub>x</sub>C<sub>6</sub> contribution, suggesting that  
313 plating is not fully quantified by this metric (Fig. S28). The source of this error may be visualized in the  
314 1C charging profiles for a representative cell in Fig. 4b, recalling that 1C cycle 5 is followed by 6C  
315 cycles 1 and 2 then 1C cycle 6, and that 1C cycle 10 is followed by 6C cycles 3 and 4, and so forth. The  
316 profiles show that for the first few fast charging cycles, the voltage segment corresponding to early  
317 graphite lithiation shifts to the right (dashed box). Physically, the shift indicates a change in the  
318 electrode potential windows during charge and the removal of additional cyclable lithium<sup>46</sup> from the

319 graphite to compensate lithium losses from plating. Thus, we believe this graphite SOC shift should  
320 estimate losses not captured by the 1C capacity loss, which conversely manifests by the high-voltage  
321 capacity shifting to the left (solid box).  
322

323 The SOC shift ( $\Delta X$ ) and capacity loss ( $\Delta C$ ) are reported for each pair of 6C fast charging cycles in Fig.  
324 4c (see Methods for detailed calculation). The combined loss for each pair of cycles is about the same,  
325 which is reasonable because i) the amount of loss per pair is small,  $\sim 1\%$  of the total capacity, and ii) the  
326 cell aging that might promote increased plating over time is counterbalanced by increasing CCCV  
327 charge times, which lowers the average C-rate (Fig. S21). The graphite SOC shift contribution decreases  
328 from about 50% of losses for 6C Cycles 1-2 to  $\sim 0\%$  for Cycles 25-26 and beyond as the residual lithium  
329 in the graphite is consumed, highlighting the importance of this metric for accurate early plating  
330 quantification. Fig. S25 shows Fig. 4c for all cells, an impressive visualization that indicates accurate  
331 loss quantification with single cycle resolution.  
332

333 Fig. 4c shows significantly less titrated Li for the FEC electrolyte cells compared to the 0% FEC cells,  
334 as anticipated from Figs. 3 and 4a electrochemical measurements and electrode images (Fig. S26). There  
335 is also a strong correlation between the sum of the 6C losses (from Fig. 4c) and titrated Li. For the 0%  
336 FEC electrolyte, the fraction of the loss accounted for by titrated Li is about 81% (Fig. 4c inset),  
337 comparable to other studies of dead Li using similar electrolytes<sup>12,13</sup>. This leads us to suspect that the  
338 majority of the 6C losses are indeed due to irreversible Li plating, but note that this metric may include  
339 losses from other fast-charging degradation such as SEI formation or electrode active material loss. The  
340 Li fraction with FEC is lower and decreases slightly from about 40% to 20% with increasing  
341 concentration, again highlighting the potential FEC advantage for avoiding metallic Li buildup during  
342 cell malfunction. Still, these values are notably higher than the  $\sim 10\%$  fractional dead Li that others have  
343 observed for slow Li deposition on Cu for similar FEC electrolytes<sup>12,33,47</sup>, emphasizing phenomena  
344 unique to fast charging and the need to understand loss mechanisms besides dead Li formation.  
345

346 Finally, the titration results unveil a route for estimating irreversible Li as a function of SOC in full-cells  
347 to allow direct comparison with half-cell results. The combined 1C capacity loss and 1C graphite SOC  
348 shift ( $\Delta C + \Delta X$ ) was a strong predictor for titrated Li for the 0% FEC electrolyte, so we then designed a  
349 protocol alternating two 1C charge cycles with two fast charging cycles to X% SOC, where X is  
350 increased by 5% for each iteration (Fig. 5a). Two cycles of each step were performed to benefit the  
351 technique sensitivity and reliability (see Fig. S30). The 1C capacity changes between fast charging steps  
352 ( $\Delta C$ ) correspond to losses from only those X% SOC cycles. Similarly, the 1C graphite SOC shift ( $\Delta X$ ) is  
353 calculated for each X% SOC fast charge step, and the combined loss is shown in the bottom of Fig. 5a,  
354 as in our previous analysis. This metric is shown for representative cells at various C-rates, and the x-  
355 axis denotes the SOC cutoff of the previous 2 fast charge cycles that are analyzed. For the full-cells, the  
356 rates and SOC are defined with respect to the nominal 3-4.2V C/10 charge capacity, and were selected  
357 so that identical graphite current densities are applied for comparison with 3C to 6C rates in the half-  
358 cells (see Supplementary Note S6).  
359

360 We then transform the data in Fig. 5a to estimate irreversible Li plating in full-cells and provide a direct  
361 comparison with the half-cells in Fig. 5b. The transformation entails i) subtracting baseline losses  
362 observed for fast charging at low SOC prior to the plating onset, as in Fig. 1b (Fig. S32), ii) normalizing  
363 the loss to the active graphite capacity, as in Fig. 1c, and dividing by 2 to account for 2 cycles to each  
364 SOC, and iii) converting the x-axis from full-cell SOC to graphite lithiation (avg. x in  $\text{Li}_x\text{C}_6$ ) by  
365 differential voltage profile analysis (see Fig. S34). We assume that 100% of the baselined  $\Delta C + \Delta X$  data  
366 corresponds to irreversible Li plating capacity. A striking similarity is the shape of the Li|Gr and  
367 Gr|NMC curves, which extends our hypothesis from Fig. S10 of universal physics for Li plating



368 regardless of counter electrode selection. Another interesting observation is that the spacing of the Li|Gr  
369 curves have a similar C-rate dependence as those of the Gr|NMC, which reveals a route for empirically  
370 scaling the half-cell data to predict full-cell behavior with limited full-cell measurements (Fig. S35).  
371 Even without this adjustment, however, the half-cells show average Li plating onset SOC (defined again  
372 as 0.05% irreversible Li) within 3% of full-cells for the 20.1 mA/cm<sup>2</sup> rate and within 6% for 13.4  
373 mA/cm<sup>2</sup>, suggesting the Fig 2a-b Li|Gr measurements at the higher current densities (4C and above) are  
374 the most translatable for full-cells. We also offer some physical explanations for the plating onset  
375 differences based on prior modeling in Supplementary Note S7.

376  
377 As the final step of technique verification, the graphite electrodes were titrated for comparison with the  
378 cumulative irreversible Li estimated for each cell (Fig. 5c), determined by summation of the  $\Delta C + \Delta X$   
379 values of Fig. 5a for each curve after the described baselining. The strong linear correlation ( $R^2 = 0.991$ )  
380 with near unity slope further suggests that the method accurately predicts plating amounts and estimates  
381 that, on average, 94% of irreversible Li plating exists in the form of electrically isolated Li<sup>0</sup> and other  
382 titration Li, with the remaining 6% as Li<sup>+</sup>-containing SEI species. The application of this protocol for  
383 electrolyte engineering in full-cells should be investigated in future works, but we note that this 1.2 M  
384 LiPF<sub>6</sub> in 3:7 EC:EMC electrolyte offers favorable Li detection properties and is well-suited for  
385 immediate subsequent studies. There is vast opportunity to quantify the effects of electrode porosity,  
386 loading, temperature, composition, and heterogeneity on Li plating to inform cell manufacturing, quality  
387 control, and battery operation.

## 388 389 Conclusions

390  
391 Lithium plating is a nearly universal challenge for battery performance and operation, but its difficulty  
392 to detect has limited robust experimental studies. We have developed and verified high-throughput  
393 cycling techniques to quantify lithium plating in-situ in Li|Graphite and Graphite|NMC cells, and the  
394 abundant data have led to physical insights of plating behavior, electrochemical modeling  
395 improvements, cell design heuristics, routes toward data-driven plating models, and electrolyte  
396 engineering strategies. Going forward, we believe that widespread reporting of irreversible Li plating  
397 curves and onset SOC will help quantify the tradeoffs of novel battery design or operation approaches  
398 for fast charging, as well as lead to improved fundamental understanding. We hope these techniques are  
399 employed by academic and industry researchers and continually adapted to further reduce experiment  
400 time, consider battery aging effects on plating, transfer effectively to other cell formats, and study  
401 nascent battery chemistries.

## 402 403 Methods

404  
405 **Materials.** Electrolytes were made with ethyl methyl carbonate (EMC), ethylene carbonate (EC),  
406 fluoroethylene carbonate (FEC), and lithium hexafluorophosphate (LiPF<sub>6</sub>) from Gotion Inc and used  
407 within a week of preparation. Composite graphite electrodes were obtained from the Argonne National  
408 Laboratory CAMP facility with 91.83 wt% Superior Graphite SLC 1506T, 2 wt% Timcal C45 carbon, 6  
409 wt% Kureha 9300 PVDF binder, 0.17 wt% Oxalic Acid on Cu foil (10  $\mu$ m). Various combinations of  
410 [thickness, loading, porosity] were used based on application and availability, A1 = [47  $\mu$ m, 2.1 mAh  
411 cm<sup>-2</sup>, 37.4%], A2 = [70  $\mu$ m, 3.1 mAh cm<sup>-2</sup>, 38.2%], A3 = [70  $\mu$ m, 3.35 mAh cm<sup>-2</sup>, 34.4%], A4 = [85  $\mu$ m,  
412 3.75 mAh cm<sup>-2</sup>, 35.4%]. Plating onset and temperature experiments (Figs. 1-2) used anodes A1 and A2.  
413 Plating reversibility experiments (Fig. 3) used A2. Full-cell plating experiments and Full-cell/half-cell  
414 validation (Figs. 4-5) used A3. Empirical fit prediction testing (Fig. S11) used A4. The composite  
415 LiNi<sub>0.5</sub>Mn<sub>0.3</sub>Co<sub>0.2</sub>O<sub>2</sub> cathode was 90 wt% Toda NMC532, 5 wt% Timcal C45 carbon, 5 wt% Solvay

416 5130 PVDF binder, with  $2.8 \text{ mAh cm}^{-2}$  and targeted P:N ratio 1:1.2 with anodes A2-A3,  $71 \mu\text{m}$  coating  
417 on  $20 \mu\text{m}$  Al foil, 35.6% porosity. All electrodes were dried at  $120^\circ\text{C}$  under vacuum overnight before  
418 transferring directly to the glovebox.

419 Hohsen CR2032 coin cells were used for all experiments, with  $30 \mu\text{L}$  total electrolyte added  
420 quickly in 3 separate  $10 \mu\text{L}$  aliquots to ensure uniform wetting while avoiding evaporation. Graphite  
421 electrodes were  $15 \text{ mm}$  diameter punches, paired with either  $14 \text{ mm}$  dia. Li foil ( $0.7 \text{ mm}$  thickness, MTI  
422 Corp) or  $14 \text{ mm}$  dia. NMC and separated by a single  $18 \text{ mm}$  dia. Celgard 2500 separator ( $25 \mu\text{m}$   
423 monolayer polypropylene). The molar ratio of Li:Gr in half-cells is greater than 30:1 for all loadings  
424 (see Note S2). All assembly/disassembly was performed in an argon-filled glovebox with  $\text{O}_2 < 1.0 \text{ ppm}$ ,  
425  $\text{H}_2\text{O} < 0.5 \text{ ppm}$ . Electrochemical testing used Biologic MPG-200, VMP3, and BCS-810 potentiostats  
426 with CCH-8 coin cell holders at temperature control in Thermotron environmental chambers. Coin-cell  
427 temperature rise from the chamber setpoint is expected to be minimal ( $< 5^\circ\text{C}$ ) during cycling (see Note  
428 S1). Cycling protocols were implemented with Biologic's EC-Lab software.

429 **SOC-sweep testing for Li|Graphite cells** (Figs. 1, 2, 3a, S11). One slow formation cycle entails C/10  
430 intercalation to  $0.01 \text{ V}$  and C/5 deintercalation to  $1.5 \text{ V}$  with 5-minute rest between each step. The  
431 experimental graphite capacity is determined from the discharge capacity of the 3<sup>rd</sup> and final C/10  
432 formation cycle and used to set the C-rates and SOC cutoffs for subsequent cycling. We refer to graphite  
433 intercalation as 'charging' and deintercalation as 'discharging' for consistency with language used for  
434 full-cell commercial lithium-ion batteries, even though the intercalation process is spontaneous in the  
435 Li|Graphite cell configuration. Next, each cell underwent 5 fast formation cycles of 4C charge to 10%  
436 SOC and C/5 discharge to  $1.5\text{V}$  with 15-minute rest between current steps (see Fig. S2). Last, the cell  
437 undergoes the SOC-sweep cycling in which the charge capacity is increased 5-10% SOC for each  
438 subsequent cycle, with each charge step alternated with C/5 discharge to  $1.5\text{V}$ , and a 30-minute rest  
439 between current steps. The SOC window and step size was selected based on the expected plating onset  
440 SOC; for later expected onsets, a step size of 10% was selected to cover large SOC range while  
441 minimizing experiment time (see Table S2). For high-temperature experiments, the oven temperature  
442 was increased from  $25^\circ\text{C}$  to the target temperature during the 5 fast charging formation cycles. For Fig.  
443 3a comparing electrolyte compositions, the first formation cycle used C/20 instead of C/10 to clearly  
444 articulate dQ/dV features, seen in Fig. 3d. Typically 3 cells were run initially at each condition in Figs.  
445 1, 2, 3a, and S11, but the number of cells reported varies between 2 and 5 (e.g., see Fig. 2a-f, bottom left  
446 of each panel). An additional set of 2-3 cells may have been run for better data statistics or to make up  
447 for data that was excluded due to indicators of poor cell performance resulting from imperfections in  
448 manual cell preparation. For a description of such 'bad cells,' see Fig. S1.3.

449 **Electrochemical Modeling** (Figs. 2, 3g). Additional notes to supplement the main text model  
450 description: The universal plating reversibility was previously estimated to be roughly 70% ( $\eta = 0.7$ )  
451 under fast charge conditions and modest amounts of plating<sup>13</sup> and is a value previously observed at low  
452 temperature ( $-20^\circ\text{C}$ ) and overcharge rate (C/10) plating conditions<sup>34</sup>. Irreversible lithium plating is  
453 determined from multiplying  $(1 - \eta)$  by the modeled plating amount. All electrolyte transport properties  
454 are taken from Idaho National Laboratory's Advanced Electrolyte Model (AEM)<sup>48</sup> and use empirical fits  
455 as a function of salt concentration and temperature<sup>24</sup>. The anode and separator Bruggeman coefficient  
456 are estimated as 2.2-2.3 and 2.0, respectively, based on detailed microstructure  
457 characterization/modeling and impedance spectroscopy using a blocking electrolyte<sup>49</sup>. The exchange  
458 current density and solid-state diffusion are estimated based on extensive fitting to electrochemical data  
459 including full-cells, half-cells, and 3-electrode test setups from within the US Department of Energy  
460 XCEL fast charge program<sup>9,24,25</sup>. The exchange current density for the lithium working electrode and  
461 lithium plating within the graphite anode are both set to  $10 \text{ A/m}^2$  as in our prior report<sup>13</sup>. The half-cell  
462 and full-cell models are written in C++ and use the SUNDIALS Suite of Nonlinear and  
463 Differentiable/Algebraic Equation Solvers<sup>50</sup>.

464 **Lithium plating reversibility on graphite protocol** (Fig. 3b). After 3 C/10 formation cycles and  
 465 determining the experimental capacity, the graphite is intercalated at C/3 to 0.01 V and held 1 h or until  
 466 current drops below 10  $\mu\text{A}$  (C/500) followed by immediate C/5 discharge to 1.5V. This cycle is to  
 467 determine the coulombic efficiency for complete graphite lithiation in the absence of lithium plating.  
 468 The following 5 cycles are identical except after the intercalation, intentional overcharge (Li plating)  
 469 occurs at the selected C-rate (0.2C-4C) and capacity (10-30% SOC), both specified relative to the  
 470 experimental full graphite intercalation capacity. A representative voltage profile for this cycling  
 471 protocol is provided in Fig. S16. The specific plating reversibility calculation is detailed in Eqn. 3 and  
 472 corresponding text.

473 **Incremental plating reversibility calculation** (Fig. 3f). The data from Fig. 3c report the plating  
 474 reversibility for 10%, 20%, and 30% overcharge ( $\eta_{10}$ ,  $\eta_{20}$ ,  $\eta_{30}$ ) collected with separate coin cells and  
 475 these values can be algebraically manipulated to estimate the reversibility for Li deposited between 10-  
 476 20% SOC ( $\eta_{10-20}$ ) and 20-30% SOC ( $\eta_{20-30}$ ):

$$(4) \text{ (reversible plating 0-20\% SOC)} = \text{(reversible plating 0-10\% SOC)} + \text{(reversible plating 10-20\% SOC)}$$

477

$$(4) \eta_{20}(20\% \text{ SOC}) = \eta_{10}(10\% \text{ SOC}) + \eta_{10-20}(10\% \text{ SOC})$$

480

$$(5) \eta_{10-20} = \frac{0.2 \eta_{20} - 0.1 \eta_{10}}{0.1}$$

482

Similarly,

483

$$(6) \eta_{20-30} = \frac{0.3 \eta_{30} - 0.2 \eta_{20}}{0.1}$$

484

485

And error bars were estimated by standard propagation of uncertainty (see text below Fig. S14).

486 **Lithium plating on copper foil** (Fig. 3f). Lithium was deposited on 15 mm Cu foil (25  $\mu\text{m}$ , MTI Corp)  
 487 from a 14 mm Li metal electrode at a current density of 4C with respect to anode A2 capacity (3.1 mA h  
 488  $\text{cm}^{-2}$ ) for 1.5 minutes (0.31 mA h  $\text{cm}^{-2}$ , 10% SOC) to mimic plating at the Graphite|separator interface  
 489 during the graphite plating reversibility experiments. Immediately after Li deposition, an oxidative C/5  
 490 current was applied until the cell voltage exceeded 1.0V. The capacity ratio of the current stripping and  
 491 plating steps is the reported reversibility. This cycle was repeated 5 total times with 10 minutes rest in  
 492 between, and the reversibility reported is an average value from cycles 3-5 (2+ cells for each  
 493 electrolyte), which exhibit stabilized CE value relative to the first 2 cycles (Fig. S15).

494 **Graphite|NMC532 full-cell electrolyte testing** (Fig. 4a-c). The experimental full-cell capacity is  
 495 determined from the discharge capacity of the 3<sup>rd</sup> and final C/10 formation cycle and used to set the C-  
 496 rates and capacity cutoffs for subsequent cycling. One slow formation cycle entails C/10 charge to 4.2 V  
 497 and C/5 discharge to 3.0 V. All full-cell cycles include 5-minute rests between current steps. Next, 20  
 498 additional formation cycles are performed with 1C charge to 4.2V and 1C discharge to 3.0 V, holding  
 499 until the current drops below C/5 on discharge ( $\sim 5$  min). Cell performance is analyzed from the  
 500 following sequence: 5 cycles of **a**) 1C CCCV charge to 4.2V, holding until C/5 ( $\sim 10$  min), and 1C  
 501 discharge to 3.0 V holding until C/5, alternating with 2 cycles of **b**) 6C CCCV charge to 4.2V, holding  
 502 until 80% SOC (about 12 min total charge), then 1C discharge to 3.0 V holding until C/5. This sequence  
 503 is repeated 20 times for a total of 100 1C cycles and 40 6C cycles. To prepare full-cells for titrations, the  
 504 final step is a C/5 deep discharge down to 0.1 V to remove residual active lithium from the graphite.

505 **Electrochemical data analysis** (Fig. 4b-d), Electrode voltage (V) shifts or capacity (Q) changes in full-  
 506 cells are often characterized by monitoring the capacity (x-position) at which local extrema in  
 507 differential voltage curves (dV/dQ, y-axis) occur<sup>51</sup>. Here, the dV/dQ vs. Q curve shift is alternatively  
 508 calculated from the capacity at which  $Q_0 \cdot dV/dQ = 1.0$  V, defined as X, where  $Q_0$  is the initial cell  
 509 capacity (Fig. S23). The graphite SOC shift ( $\Delta X$ ) between Cycles 5 and 6, which corresponds to 6C  
 510

511 Cycles 1+2 in Fig. 4c, is calculated with the following equation, and the subscript denotes the 1C cycle  
 512 number:

$$513 \quad (7) \quad \Delta X_{6C \text{ cycles } 1 \& 2} = (X_7 - X_5) - (X_5 - X_3)$$

514  
 515 This equation is used instead of  $\Delta X = (X_6 - X_5)$  to account for transient behavior of the 1<sup>st</sup> 1C cycle  
 516 after fast charging (here, Cycle 6) and to subtract nominal SOC shift that would also occur in 1C cycles,  
 517  $(X_5 - X_3)$ , reducing contributions from cell aging unrelated to fast charging. Fig. S24 provides thorough  
 518 justification for this formula. Generalizing to determine  $\Delta X$  that occurs for the 2 6C cycles n and (n+1)  
 519 that occur between 1C cycles N and (N+1) yields:

$$520 \quad (8) \quad \Delta X_{6C \text{ cycles } n \& (n+1)} = (X_{N+2} - X_N) - (X_N - X_{N-2})$$

521  
 522 For 1C cycle numbers:  $N = [5, 10, 15, \dots, 90, 95]$  and  
 523 Corresponding 6C cycle numbers:  $n = (2N/5) - 1 = [1, 3, 5, \dots, 35, 37]$   
 524  
 525

526 Similarly, the changes in 1C discharge capacity reported in Fig. 4c,  $\Delta C$ , are calculated by the following  
 527 where C is the discharge capacity for the Nth 1C cycle:

$$528 \quad (9) \quad -\Delta C_{6C \text{ cycles } n \& (n+1)} = (C_{N+2} - C_N) - (C_N - C_{N-2})$$

529  
 530 For both  $\Delta X$  and  $\Delta C$ , the values for 6C cycles 39&40 are assumed identical to cycles 37&38 because  
 531 additional 1C cycles were not performed after the 2 final fast charge cycles.  
 532

533 **Graphite|NMC532 SOC-sweep Li plating quantification** (Fig. 5a-c). For these cells, the experimental  
 534 full-cell capacity,  $C_{full-cell}$ , was fixed at 4.30 mAh (100% SOC, 2.80 mAh/cm<sup>2</sup>, average of previous  
 535 experiments) to fix the current density applied to the graphite electrodes for comparison with  
 536 Li|Graphite cells. **1. Cycling Protocol.** **a)** 3x slow formation cycles 3.0-4.2V as described above. **b)** 10x  
 537 1C formation cycles CC charge to 4.2V, 1C CCCV discharge to 3.0V hold until C/20. Holding until  
 538 C/20 was selected to minimize the graphite lithiation at the start of charge for the best comparison with  
 539 Li|Graphite cell measurements. **c)** 1x cycle C/10 charge to 4.2V, 1C discharge to 3.0V hold until C/20.  
 540 The charging step is used for dV/dQ analysis to determine the active graphite capacity and graphite  
 541 lithiation at the start of charge (Fig. S34). **d)** Cell performance was analyzed from the following  
 542 sequence (see Fig. S29 for representative voltage profiles during this protocol): 2 cycles of **i)** 1C CCCV  
 543 charge to 4.2V, holding until C/5 (~10 min), and 1C discharge to 3.0 V holding until C/20, alternating  
 544 with 2 cycles of **ii)** fast charge at the specified C-rate constant-current until X% SOC, then 1C discharge  
 545 to 3.0 V holding until C/20 and **iii)** repeating from sequence i) except increasing the fast charging SOC  
 546 cutoff of ii) by 5%. After the final set of fast charging cycles, 2 additional 1C cycles are performed. **iv)**  
 547 C/5 deep discharge to 0.1V to prepare for titrations. **2. Data analysis.** **a)** The graphite SOC shift  $\Delta X$  and  
 548 capacity loss  $\Delta C$  for each pair of fast charging (FC) cycles was calculated by taking the difference of the  
 549 2<sup>nd</sup> cycle of each pair of 1C cycles. Only the 2<sup>nd</sup> cycle was analyzed due to transient capacity and  
 550 coulombic efficiency behavior for the 1<sup>st</sup> 1C cycle of each set after fast charge (Fig. S30) . Inspired by  
 551 the analysis described for the 140-cycle full-cell methods above:  
 552

$$553 \quad (10) \quad \Delta X_{fast \text{ charge at } XC \text{ to } X\% \text{ SOC}} = (X_{2nd \text{ 1C cycle after FC}} - X_{1C \text{ cycle before FC}})$$

$$554 \quad (11) \quad -\Delta C_{fast \text{ charge at } XC \text{ to } X\% \text{ SOC}} = (C_{2nd \text{ 1C cycle after FC}} - C_{1C \text{ cycle before FC}})$$

555  
 556 Note: in contrast to the 140-cycle full-cell equations for  $\Delta X$  and  $\Delta C$ , here there is no correction term that  
 557 subtracts losses for 1C aging. **b)** This is because for the next analysis step, to estimate irreversible Li  
 558 plating, the  $\Delta C + \Delta X$  data from part **(a)** (seen in Fig. 5a) is baselined to subtract losses from aging that

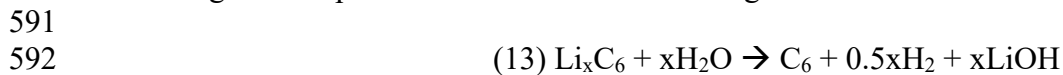
559 are not related to lithium plating. This process is illustrated and discussed thoroughly in Fig. S32. **c)**  
560 Finally, to convert full-cell SOC at the end of charge (x-axis, Fig. 5a) to graphite lithiation at end of  
561 charge (x-axis, Fig. 5b), the following equation is used:  
562

$$563 \quad (12) \quad x \text{ in } Li_xC_6 = x_{initial} + SOC_{full-cell} \cdot \frac{C_{full-cell}}{C_{active\_graphite}}$$

564  
565 Where  $x_{initial}$  is the initial graphite lithiation at the beginning of charge and  $C_{active\_graphite}$  is the active  
566 graphite capacity, both determined from dV/dQ analysis (Fig. S34). Uncertainty propagation analysis  
567 indicates that the error induced by this transformation is no larger than 1% lithiation (see Note S5).

568 **Electrode extraction, imaging, mass-spectrometry titration, and titration calibrations** (Fig. 4c, 5c).  
569 Graphite electrodes from full-cell experiments were extracted with a Hohsen Coin Cell Disassembling  
570 Tool in the glovebox and imaged with a wireless handheld microscope (TAKMLY) before transferring  
571 to individual 6 mL vials (Metrohm). The vials were placed under active vacuum for 5 minutes before  
572 crimp-sealing the septum caps. Electrodes were extracted within 24 h of cycling completion and were  
573 stored in the glovebox for up to 3 days before titration. Rinsing the electrodes 2x with dimethyl  
574 carbonate before vial storage was found to have minimal effect on dead Li measurements, so the  
575 majority of samples were not rinsed (Fig. S28).

576 The Ar-filled sample vials were removed from the glovebox, quenched with 0.5 mL of nitrogen-  
577 sparged deionized water, swirled for 10 seconds, and then attached to the mass spectrometry titration  
578 (MST) system using a novel syringe needle attachment featuring an adapter (Valco, part # ZBUMLPK)  
579 from 1/16" stainless steel tubing to Luer-lock (Fig. S17). The MST system draws 2 mL of the vial  
580 headspace every 2 minutes, refilling the balance with ultra-high purity Argon, using a constant system  
581 pressure of  $1030 \pm 10$  Torr. After about 40 minutes, or when the H<sub>2</sub> signal ( $m/z = 2$ ) had decayed to its  
582 initial value (Fig. S18), the next vial was attached. This improved vial-swapping design along with  
583 smaller vial volume resulted in a three-fold throughput increase from our previous work<sup>13</sup>, and the signal  
584 strength suggests that 50 ng of Li metal (equivalent to 0.2  $\mu$ Ah total capacity) can be confidently  
585 quantified with each headspace sample precise to 10 ng (Fig. S19). The calibration process that  
586 quantifies the linear relationship between the H<sub>2</sub> signal and the partial pressure of H<sub>2</sub> is detailed in  
587 Supplementary Note S4 and Fig. S20. To safely and precisely generate small quantities of H<sub>2</sub> in the 6  
588 mL vials, graphite electrodes were formed and lithiated to known SOC (10-30%) in half-cells, extracted  
589 as detailed above, cut into pieces with known mass fractions of the entire 15 mm electrode, and titrated,  
590 assuming the complete conversion of the following reaction:



592  
593  
594 The amount of titrated Li in the manuscript is presented as a capacity by converting the moles of H<sub>2</sub>  
595 assuming 1 mol oxidizable Li species per 0.5 mol H<sub>2</sub>, and 1 mol e<sup>-</sup> per mol Li.

596 Even in the absence of lithium plating, cycled graphite electrodes are expected to have nonzero  
597 titrated Li due to the presence of residual Li<sub>x</sub>C<sub>6</sub><sup>13</sup> that is either electrically isolated or not fully removed  
598 during the deep discharge step. This nonzero amount was quantified with controls for each type of  
599 experiment and subtracted from the values reported in Figs. 4 and 5. For Fig. 4 experiments, the value  
600 was  $0.012 \pm 0.002$  mAh/cm<sup>2</sup> (see Fig. S27), and for Fig. 5 experiments it was  $0.019 \pm 0.001$  mAh/cm<sup>2</sup>  
601 (Fig. S31), both of which are <1% of the total graphite lithiation capacity of 3.25 mAh/cm<sup>2</sup>.

602  
603  
604

## 605 Author Correspondance

606 Correspondance and requests for materials should be directed to [bmcclosk@berkeley.edu](mailto:bmcclosk@berkeley.edu).

607

608

## 609 Data Availability

610 All data supporting the findings in this study are available within the paper and Supplementary

611 Information file. Source data for all paper figures is provided.

612

## 613 Acknowledgements

614 This work was largely supported by the Vehicle Technologies Office of the U.S. Department of Energy  
615 under the XCEL Fast Charging Program (eXtreme Fast Charge Cell Evaluation of Lithium ion Batteries,  
616 XCEL). Part of this work was authored by the National Renewable Energy Laboratory, operated by the  
617 Alliance for Sustainable Energy, LLC, for the U.S. Department of Energy (DOE) under Contract DE-  
618 AC36-08GO28308. H.K.B., D.E.B., and E.J.M. acknowledge support from the National Science  
619 Foundation Graduate Research Fellowship Program under Grant DGE 1106400. T-Y.H. gratefully  
620 acknowledges support collectively from both Ministry of Education in Taiwan and UC Berkeley College  
621 of Chemistry through the Taiwan Fellowship Program. The authors thank S. Trask, A. Jansen, A.  
622 Dunlop, and B. Polzin from the Argonne National Laboratory Cell Analysis, Modeling, and Prototyping  
623 (CAMP) facility for providing laminate electrodes used in the study. Z.M.K. thanks Jeffrey Heo for  
624 assistance with Fig. 4e design.

625

## 626 Author Contributions

627 **Z.M.K.** conceived ideas, performed experiments, developed methods, wrote analysis code, wrote  
628 manuscript and SI. **B.M.W.** developed Fig. 4 methods and analysis with Z.M.K. and provided  
629 continuous project and manuscript feedback. **A.V.** and **A.M.C.** performed EChem modeling simulations  
630 and wrote corresponding manuscript/SI sections. **T-Y.H.** helped Z.M.K. build titration syringe  
631 attachment. **H.K.B.** helped experiment design for Li plating on copper and electrolyte conductivity  
632 measurements. **M.J.C.** and T-Y.H. provided feedback and assistance with titrations. **D.E.B.** and **E.J.M.**  
633 provided project feedback, troubleshooting ideas, and mentorship. **A.M.C.** also conceived Fig. 2  
634 experiments with Z.M.K., led EChem model modifications, and provided continuous project feedback.  
635 **B.D.M.** was lead project supervisor, conceived ideas, and was primary manuscript editor. All authors  
636 edited and provided feedback on manuscript.

637

## 638 Competing interests

639 The authors declare no competing interests.

640

## 641 Tables

642

643

**Table 1 | Quantifying parameter effects on plating onset**

Empirical expression	Values at base conditions <sup>†</sup>
$\left(\frac{\partial y}{\partial c}\right)_{x,T} = \frac{\alpha}{1 + \gamma T}$	-9 % SOC/1C
$\left(\frac{\partial y}{\partial x}\right)_{T,c} = \frac{\beta}{1 + \gamma T}$	-20 % SOC/(mAh·cm <sup>2</sup> )
$\left(\frac{\partial y}{\partial T}\right)_{c,x} = \frac{\gamma}{1 + \gamma T}(1 - y)$	0.7 % SOC/1°C

<sup>†</sup>Partial derivatives of Equation 2 are evaluated at 30°C, 3.0 mAh/cm<sup>2</sup>, and 4C with fitted parameters reported in the Fig. 2h caption.

## 644 Figure Captions

645

646 **Fig. 1 | Determining irreversible Li plating as a function of charge rate and length.** **a**, SOC-sweep  
647 cycling protocol to test charging performance at 4C to varied states-of-charge. **b**, CE's from the cycling  
648 in (a) show a drop around 40% SOC, indicating the accumulation of irreversible Li plating. **c**, The CE's are  
649 recast as an irreversible lithium capacity by subtracting all CE's from the high-CE plateau (dashed  
650 line) and multiplying the resulting CIE% by the normalized charge capacity. Additional data are  
651 overlaid for this condition (3.1 mAh/cm<sup>2</sup>, 25°C) with charge rates of 6C (n=4), 5C (n=2), 4C (n=4), 3C  
652 (n=3), and 2C (n=3). For this electrode, 1% is ~31 μAh/cm<sup>2</sup> but varies with cell capacity ( $\bar{x} = 3.11$ ,  $\sigma =$   
653 0.05 mAh/cm<sup>2</sup>).

654

655 **Fig. 2 | Irreversible Li plating and plating onsets with modeling.** **a-f**, Irreversible lithium averages  
656 and standard deviations for rates 2C-6C for graphite loadings of 3.1 mAh/cm<sup>2</sup> (a-c) and 2.1 mAh/cm<sup>2</sup> (d-  
657 f) at 25°C (a,d), 35°C (b,e), and 45°C (c,f). Data are interpolated with a cubic spline and number of cells  
658 n are listed for each condition (see Fig. S3.3). Electrochemical model simulations are in dashed lines and  
659 assume 70% plating reversibility. Horizontal lines indicate the threshold used to define the lithium  
660 plating onset SOC, 0.05% or 1.0-1.5 μAh/cm<sup>2</sup> irreversible Li. The inset in (e) illustrates that the onsets  
661 are the x-values where the average curves intersect y=0.05%. **g**, Plating onset comparisons of model  
662 and experiment for the data in (a)-(f). The experiment error bars in (g)-(h) are calculated from the  
663 intersection of y=0.05 with the upper and lower curves bounding each shaded region in (a)-(f). **h**, The  
664 data-driven fitting of Eqn. 2 overlaid with experiment plating onsets, generated with parameters  $\alpha = -$   
665 0.16 SOC/1C,  $\beta = -0.315$  SOC/mAh·cm<sup>-2</sup>,  $\gamma = 0.025$  (°C)<sup>-1</sup>, and  $\varepsilon = 1.70$  SOC.

666

667 **Fig. 3 | Electrolyte engineering to reduce irreversible Li plating.** **a**, Irreversible Li in Li|Graphite  
668 cells using the Fig. 1 protocol for varied weight percent (X) FEC in 1.2 M LiPF<sub>6</sub> electrolyte, resulting in  
669 FEC:EC:EMC wt% ratios of X:(30-X):70. Conditions: 4C rate, 3.1 mAh/cm<sup>2</sup>, 25°C. **b**, Overcharge  
670 protocol to rigorously determine the lithium plating reversibility for high-rate plating. The intercalation  
671 capacity (Q<sub>int</sub>), plating capacity (P), and overcharge irreversible capacity (Q<sub>irrev</sub>) are used in Equation 3  
672 to calculate the reversibility. See Methods for additional protocol details. **c**, Li reversibility varying the  
673 amount of 4C plating (left) and varying C-rate (right) for 20% plating, where 10% is 0.31 mAh/cm<sup>2</sup>.  
674 Error bars represent standard deviation for n=3 cycles on the same coin cell. **d**, Differential capacity  
675 curves from the first graphite lithiation at C/20 rate. **e**, Temporospacial schematic of Li plating location  
676 during 30% overcharge and sketch of associated Li plating current densities. **f**, Plating reversibility by  
677 each segment in (e) for each electrolyte composition, calculated from data in (c), compared with  
678 reversibility for the same plating capacity and rate on copper foil. Error bars for 10-20% and 20-30% are  
679 estimated with uncertainty propagation (Fig. S14). **g**, The sum of squared errors (SSE) for Li plating  
680 onsets from experiment and the electrochemical model (Fig. 2g) across all conditions vs. the plating  
681 reversibility assumed by the model.

682

683 **Fig. 4 | Full-cells electrolyte testing with dead Li estimation and titration** **a**, Graphite|NMC532 1C  
684 discharge capacity normalized to the initial (Cycle 1) value vs. cycle number, with cells undergoing two  
685 cycles of 6C CCCV to 4.2V charging to 80% SOC after five 1C cycles. The inset emphasizes capacity  
686 jumps between groups of 1C cycles due to the intermittent 6C cycles that induce Li plating. Error bars  
687 depict standard deviations across n cells. **b**, Representative 1C charging profiles throughout cycling.  
688 Insets show how the profile shifts during cycling, and phenomena associated with the shifts. **c**, Loss  
689 quantified from capacity change and graphite SOC shift. The data for 6C Cycles 1+2 is determined by  
690 analyzing 1C Cycles 3-5 (before 6C) and 7 (after, see Methods for details). **d**, Titrated Li (Li<sup>0</sup> and Li<sub>x</sub>C<sub>6</sub>)  
691 vs. the sum of the data in (c) for all cells tested in (a). The inset shows the fraction of the estimated loss  
692 accounted for by titrated Li, the position of each point relative to the dotted parity line.

693  
694  
695  
696  
697  
698  
699  
700  
701  
702  
703  
704  
705

**Fig. 5 | Determining irreversible Li in full-cells, comparison with half-cells, and titration validation.** **a**, Characterizing irreversible Li in full-cells by monitoring the normalized 1C discharge capacity with intermittent 2 cycles of constant-current fast charging to progressively higher SOC. The sum of capacity loss ( $\Delta C$ ) and graphite SOC shift ( $\Delta X$ ) from each set of fast charge cycles is shown and used to calculate the irreversible Li (see Methods). **b**, Comparing irreversible lithium on graphite with NMC (connected points, individual cells) and Li (shaded regions, averaged 3 cells) counter electrodes as a function of the expected graphite lithiation at the end of charge (graphite SOC). The full-cell SOC, the x-axis of (a), is converted to graphite lithiation as described in the Methods. The Gr|NMC532 C-rates were selected to fix the average geometric current densities experienced by graphite (10.05, 13.4, 20.1 mA/cm<sup>2</sup>) across cell formats, see Note S6. **c**, Titrated Li vs the total irreversible Li plating estimates for the graphite electrodes extracted from the Gr|NMC532 cells in (b).



## 706 References

707

- 708 1. Rashingkar, G. & Frost & Sullivan. *Global Li-ion Battery Materials Growth Opportunities*.  
709 [https://www.marketresearch.com/Frost-Sullivan-v383/Global-Li-ion-Battery-Materials-](https://www.marketresearch.com/Frost-Sullivan-v383/Global-Li-ion-Battery-Materials-14856305/)  
710 [14856305/](https://www.marketresearch.com/Frost-Sullivan-v383/Global-Li-ion-Battery-Materials-14856305/) (2021).
- 711 2. Zhang, S. S., Xu, K. & Jow, T. R. Study of the charging process of a LiCoO<sub>2</sub>-based Li-ion  
712 battery. *J. Power Sources* **160**, 1349–1354 (2006).
- 713 3. Tobishima, S. I. & Yamaki, J. I. A consideration of lithium cell safety. *J. Power Sources* **81–82**,  
714 882–886 (1999).
- 715 4. DNV-GL and Arizona Public Service. *McMicken Battery Energy Storage System Event Technical*  
716 *Analysis and Recommendations*. [https://www.aps.com/-/media/APS/APSCOM-PDFs/About/Our-](https://www.aps.com/-/media/APS/APSCOM-PDFs/About/Our-Company/Newsroom/McMickenFinalTechnicalReport.ashx?la=en&hash=50335FB5098D9858BFD276C40FA54FCE)  
717 [Company/Newsroom/McMickenFinalTechnicalReport.ashx?la=en&hash=50335FB5098D9858B](https://www.aps.com/-/media/APS/APSCOM-PDFs/About/Our-Company/Newsroom/McMickenFinalTechnicalReport.ashx?la=en&hash=50335FB5098D9858BFD276C40FA54FCE)  
718 [FD276C40FA54FCE](https://www.aps.com/-/media/APS/APSCOM-PDFs/About/Our-Company/Newsroom/McMickenFinalTechnicalReport.ashx?la=en&hash=50335FB5098D9858BFD276C40FA54FCE) (2020).
- 719 5. Arora, P., Doyle, M. & White, R. E. Mathematical Modeling of the Lithium Deposition  
720 Overcharge Reaction in Lithium-Ion Batteries Using Carbon-Based Negative Electrodes. *J.*  
721 *Electrochem. Soc.* **146**, 3543 (1999).
- 722 6. Tang, M., Albertus, P. & Newman, J. Two-Dimensional Modeling of Lithium Deposition during  
723 Cell Charging. *J. Electrochem. Soc.* **156**, A390 (2009).
- 724 7. Yang, X. G., Ge, S., Liu, T., Leng, Y. & Wang, C. Y. A look into the voltage plateau signal for  
725 detection and quantification of lithium plating in lithium-ion cells. *J. Power Sources* **395**, 251–  
726 261 (2018).
- 727 8. Ren, D. *et al.* Investigation of Lithium Plating-Stripping Process in Li-Ion Batteries at Low  
728 Temperature Using an Electrochemical Model. *J. Electrochem. Soc.* **165**, A2167–A2178 (2018).
- 729 9. Colclasure, A. M. *et al.* Requirements for Enabling Extreme Fast Charging of High Energy  
730 Density Li-Ion Cells while Avoiding Lithium Plating. *J. Electrochem. Soc.* **166**, A1412–A1424  
731 (2019).
- 732 10. Campbell, I. D., Marzook, M., Marinescu, M. & Offer, G. J. How Observable Is Lithium Plating?  
733 Differential Voltage Analysis to Identify and Quantify Lithium Plating Following Fast Charging  
734 of Cold Lithium-Ion Batteries. *J. Electrochem. Soc.* **166**, A725–A739 (2019).
- 735 11. Paul, P. P. *et al.* A Review of Existing and Emerging Methods for Lithium Detection and  
736 Characterization in Li-Ion and Li-Metal Batteries. *Adv. Energy Mater.* **11**, 1–29 (2021).
- 737 12. Fang, C. *et al.* Quantifying inactive lithium in lithium metal batteries. *Nature* **572**, 511–515  
738 (2019).
- 739 13. McShane, E. J. *et al.* Quantification of Inactive Lithium and Solid–Electrolyte Interphase Species  
740 on Graphite Electrodes after Fast Charging. *ACS Energy Lett.* **5**, 2045–2051 (2020).
- 741 14. Deng, Z. *et al.* Towards autonomous high-throughput multiscale modelling of battery interfaces.  
742 *Energy Environ. Sci.* **15**, 579–594 (2022).
- 743 15. Kang, K., Meng, Y. S., Bréger, J., Grey, C. P. & Ceder, G. Electrodes with high power and high  
744 capacity for rechargeable lithium batteries. *Science (80-. )*. **311**, 977–980 (2006).
- 745 16. Qie, L. *et al.* Nitrogen-doped porous carbon nanofiber webs as anodes for lithium ion batteries  
746 with a superhigh capacity and rate capability. *Adv. Mater.* **24**, 2047–2050 (2012).
- 747 17. Smith, A. J., Burns, J. C., Trussler, S. & Dahn, J. R. Precision Measurements of the Coulombic  
748 Efficiency of Lithium-Ion Batteries and of Electrode Materials for Lithium-Ion Batteries. *J.*  
749 *Electrochem. Soc.* **157**, A196 (2009).
- 750 18. Dahn, J. R., Burns, J. C. & Stevens, D. A. Importance of coulombic efficiency measurements in R  
751 & D efforts to obtain long-lived li-ion batteries. *Electrochem. Soc. Interface* **25**, 75–78 (2016).
- 752 19. Severson, K. A. *et al.* Data-driven prediction of battery cycle life before capacity degradation.  
753 *Nat. Energy* **4**, 383–391 (2019).
- 754 20. Attia, P. M. *et al.* Closed-loop optimization of fast-charging protocols for batteries with machine

- 755 learning. *Nature* **578**, 397–402 (2020).
- 756 21. Aykol, M., Herring, P. & Anapolsky, A. Machine learning for continuous innovation in battery  
757 technologies. *Nat. Rev. Mater.* **5**, 725–727 (2020).
- 758 22. Konz, Z. M., McShane, E. J. & McCloskey, B. D. Detecting the onset of lithium plating and  
759 monitoring fast charging performance with voltage relaxation. *ACS Energy Lett.* **5**, 1750–1757  
760 (2020).
- 761 23. Adam, A., Knobbe, E., Wandt, J. & Kwade, A. Application of the differential charging voltage  
762 analysis to determine the onset of lithium-plating during fast charging of lithium-ion cells. *J.*  
763 *Power Sources* **495**, 229794 (2021).
- 764 24. Colclasure, A. M. *et al.* Electrode scale and electrolyte transport effects on extreme fast charging  
765 of lithium-ion cells. *Electrochim. Acta* **337**, 135854 (2020).
- 766 25. Finegan, D. P. *et al.* Spatial dynamics of lithiation and lithium plating during high-rate operation  
767 of graphite electrodes. *Energy Environ. Sci.* **13**, 2570–2584 (2020).
- 768 26. Robertson, D. C. *et al.* Effect of Anode Porosity and Temperature on the Performance and  
769 Lithium Plating During Fast-Charging of Lithium-Ion Cells. *Energy Technol.* **9**, 1–14 (2021).
- 770 27. Chen, Y. *et al.* Operando video microscopy of Li plating and re-intercalation on graphite anodes  
771 during fast charging. *J. Mater. Chem. A* **9**, 23522–23536 (2021).
- 772 28. Dees, D. W. *et al.* Apparent Increasing Lithium Diffusion Coefficient with Applied Current in  
773 Graphite. *J. Electrochem. Soc.* **167**, 120528 (2020).
- 774 29. Uhlmann, C., Illig, J., Ender, M., Schuster, R. & Ivers-Tiffée, E. In situ detection of lithium metal  
775 plating on graphite in experimental cells. *J. Power Sources* **279**, 428–438 (2015).
- 776 30. Gao, T. *et al.* Interplay of Lithium Intercalation and Plating on a Single Graphite Particle. *Joule* **5**,  
777 393–414 (2021).
- 778 31. Adam, A. *et al.* Development of an innovative workflow to optimize the fast-charge capability of  
779 lithium-ion battery cells. *J. Power Sources* **512**, 230469 (2021).
- 780 32. Hobold, G. M. *et al.* Moving beyond 99.9% Coulombic efficiency for lithium anodes in liquid  
781 electrolytes. *Nat. Energy* **6**, 951–960 (2021).
- 782 33. Gunnarsdóttir, A. B., Amanchukwu, C. V., Menkin, S. & Grey, C. P. Noninvasive in Situ NMR  
783 Study of ‘dead Lithium’ Formation and Lithium Corrosion in Full-Cell Lithium Metal Batteries.  
784 *J. Am. Chem. Soc.* **142**, 20814–20827 (2020).
- 785 34. Wandt, J., Jakes, P., Granwehr, J., Eichel, R. A. & Gasteiger, H. A. Quantitative and time-  
786 resolved detection of lithium plating on graphite anodes in lithium ion batteries. *Mater. Today* **21**,  
787 231–240 (2018).
- 788 35. Tanim, T. R., Dufek, E. J., Dickerson, C. C. & Wood, S. M. Electrochemical Quantification of  
789 Lithium Plating: Challenges and Considerations. *J. Electrochem. Soc.* **166**, A2689–A2696 (2019).
- 790 36. Martin, C., Genovese, M., Louli, A. J., Weber, R. & Dahn, J. R. Cycling Lithium Metal on  
791 Graphite to Form Hybrid Lithium-Ion/Lithium Metal Cells. *Joule* **4**, 1296–1310 (2020).
- 792 37. Cai, W. *et al.* The Boundary of Lithium Plating in Graphite Electrode for Safe Lithium-Ion  
793 Batteries. *Angew. Chemie - Int. Ed.* **60**, 13007–13012 (2021).
- 794 38. Mei, W., Jiang, L., Liang, C., Sun, J. & Wang, Q. Understanding of Li-plating on graphite  
795 electrode: detection, quantification and mechanism revelation. *Energy Storage Mater.* **41**, 209–  
796 221 (2021).
- 797 39. Brown, D. E., McShane, E. J., Konz, Z. M., Knudsen, K. B. & McCloskey, B. D. Detecting onset  
798 of lithium plating during fast charging of Li-ion batteries using operando electrochemical  
799 impedance spectroscopy. *Cell Reports Phys. Sci.* **2**, 100589 (2021).
- 800 40. Ho, A. S. *et al.* 3D Detection of Lithiation and Lithium Plating in Graphite Anodes during Fast  
801 Charging. *ACS Nano* **15**, 10480–10487 (2021).
- 802 41. Duangdangchote, S. *et al.* Effect of fluoroethylene carbonate on the transport property of  
803 electrolytes towards Ni-rich Li-ion batteries with high safety. *Chem. Commun.* **57**, 6732–6735

- 804 (2021).
- 805 42. Yan, S. *et al.* Regulating the growth of lithium dendrite by coating an ultra-thin layer of gold on  
806 separator for improving the fast-charging ability of graphite anode. *J. Energy Chem.* **67**, 467–473  
807 (2022).
- 808 43. Shin, H., Park, J., Sastry, A. M. & Lu, W. Effects of Fluoroethylene Carbonate (FEC) on Anode  
809 and Cathode Interfaces at Elevated Temperatures. *J. Electrochem. Soc.* **162**, A1683–A1692  
810 (2015).
- 811 44. Kazyak, E., Chen, K. H., Chen, Y., Cho, T. H. & Dasgupta, N. P. Enabling 4C Fast Charging of  
812 Lithium-Ion Batteries by Coating Graphite with a Solid-State Electrolyte. *Adv. Energy Mater.* **12**,  
813 (2022).
- 814 45. Paul, P. P. *et al.* Quantification of heterogeneous, irreversible lithium plating in extreme fast  
815 charging of lithium-ion batteries. *Energy Environ. Sci.* **14**, 4979–4988 (2021).
- 816 46. Christensen, J. & Newman, J. Cyclable Lithium and Capacity Loss in Li-Ion Cells. *J.*  
817 *Electrochem. Soc.* **152**, A818–A829 (2005).
- 818 47. Gong, C. *et al.* Revealing the Role of Fluoride-Rich Battery Electrode Interphases by Operando  
819 Transmission Electron Microscopy. *Adv. Energy Mater.* **11**, 2003118 (2021).
- 820 48. Logan, E. R., Tonita, E. M., Gering, K. L. & Dahn, J. R. A Critical Evaluation of the Advanced  
821 Electrolyte Model. *J. Electrochem. Soc.* **165**, A3350–A3359 (2018).
- 822 49. Usseglio-Viretta, F. L. E. *et al.* Resolving the Discrepancy in Tortuosity Factor Estimation for Li-  
823 Ion Battery Electrodes through Micro-Macro Modeling and Experiment. *J. Electrochem. Soc.*  
824 **165**, A3403–A3426 (2018).
- 825 50. Hindmarsh, A. C. *et al.* SUNDIALS: Suite of nonlinear and differential/algebraic equation  
826 solvers. *ACM Trans. Math. Softw.* **31**, 363–396 (2005).
- 827 51. Bloom, I. *et al.* Differential voltage analyses of high-power, lithium-ion cells 1. Technique and  
828 application. *J. Power Sources* **139**, 295–303 (2005).
- 829